Wide-Range Stability of Concurrent Load Regulation and Frequency Synchronization for a 7-Level Switched Capacitor WPT Rectifier

Spencer Cochran, *IEEE Student Member*, Daniel Costinett, *IEEE Member*
College of Electrical Engineering and Computer Science
University of Tennessee, Knoxville
Email: scochra6@vols.utk.edu

***Abstract*—Active rectifiers enhance WPT systems via tunability, high efficiency, and low waveform distortion. However, utilizing these benefits requires that two circuit characteristics are managed simultaneously: the switching frequency must be synchronized to the transmitter and the output must be regulated. Furthermore, the fundamental benefit of impedance tunability inherent to the active rectifier necessitates that this dual-objective control problem remains stable over a wide range of operating points. Either control loop can be designed in isolation, and under this premise, this work contributes a closed form derivation for the cross-coupling behaviors in the control architecture for a 7-level switched capacitor WPT system. Finally, regions of attenuated cross-coupling effects are identified and used to experimentally demonstrate wide-range control with stable output regulation and frequency synchronization.**

I. Introduction

Consumer device wireless power transfer (WPT) has gained significant traction in the last few years and is consistently included in modern flagship mobile electronics. Active rectifiers are exceptional candidates for wireless power [1]. However, any active rectifier with output regulation capabilities requires control designed to both regulate the load voltage/current and maintain switching frequency synchronization with the transmitter [2]. This dual-purpose control design problem must be addressed to leverage the benefits of active rectifiers in WPT systems.

The output can be regulated via use of an LDO [3], additional switching actions [4], or, most notably, DC-DC converters [5]. Irrespective of the approach, each of these techniques fundamentally varies the rectifier's input impedance until the output has the desired characteristic.

Without direct communication between transmitter and receiver, frequency synchronization is necessary to prevent beat-frequency variation of the rectifier impedance in steady-state. Implementation approaches include in-phase voltage actuation [6], current sensing [7], magnetic field sensing [8], or low bandwidth phase-locked loops [9]. In general, all techniques ensure that the secondary side active rectifier switches at the exact, inverter-established carrier frequency.

Previous work presents the multi-level switched capacitor rectifier (MSC, 7-level SC rectifier) as a good candidate for WPT applications [5] and accomplishes dual-loop operation at a single operating point [10]. However, the fundamental advantages associated with impedance tuning require that the dual-loop system is stable over a wide loading range. This work presents a review of the two control loops in Section II and a derivation of the cross-coupling interactions of these loops in Section III. Section IV identifies regions where the cross-coupling interactions are least prominent. Finally, Section V presents experimentally verified wide-range dual-loop control. Section VI concludes the paper.

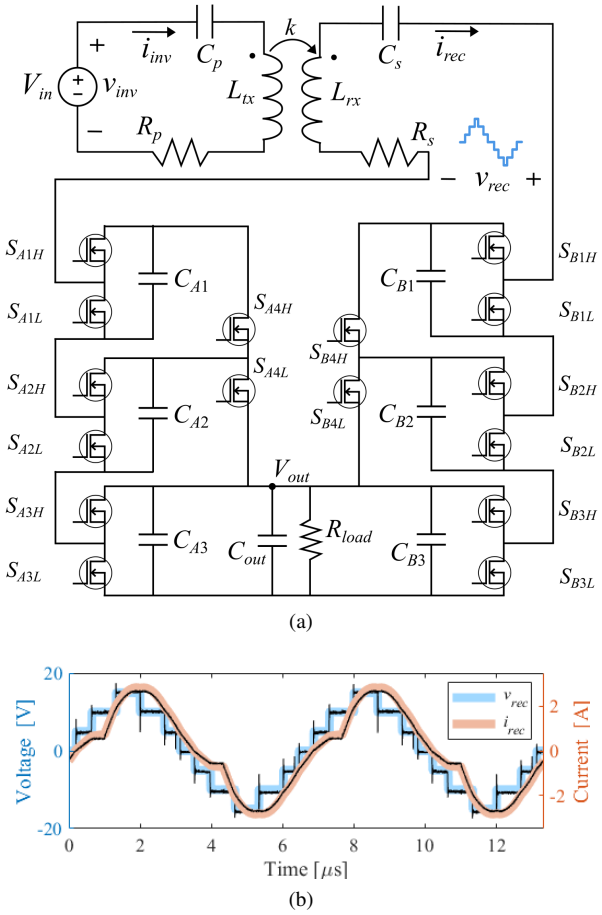

Fig. 1: (a) Wireless power circuit and (b) modeled (color) and experimental (black) waveforms.

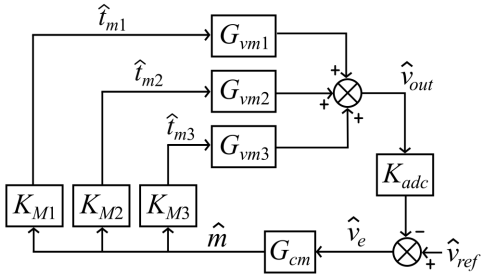

Fig. 2: Output regulation feedback loop in isolation.

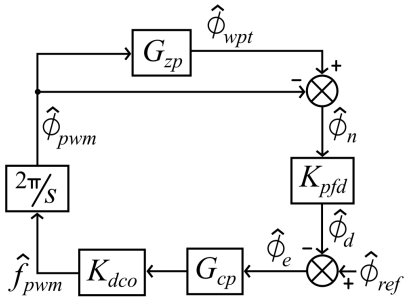

Fig. 3: Frequency synchronization feedback loop in isolation.

II. The MSC and Control Loops

The multi-level switched capacitor rectifier was previously presented in [5]. The WPT circuit including a 7-level rectifier is shown in Fig. 1a, and the accompanying waveforms are shown in Fig. 1b. The thicker, colored waveforms are the modeled rectifier waveforms using state space representation, and the thin, black waveforms are exported from an oscilloscope during experimentation. The 16 switch topology is able to reduce waveform distortion, produce exceptionally high efficiencies, tune its input impedance, and circumvent the need for bulky filter inductors [5, 11].

A. Isolated Output Regulation

Under the assumption that the rectifier switches at the exact WPT carrier frequency, the output regulation control loop of the MSC WPT system is shown in Fig. 2. The modulation index, M, is defined as $0 < M < 3.81$ for a 7-level design. The fundamental amplitude of the rectifier input voltage is related to the dc output voltage, $|v_{rec,1}| = MV_{out}$. Modulation index is varied by controlling the duty cycles of each rectifier level. Levels 1-3 that comprise the total rectifier modulation have transfer functions: G_{vm1}, G_{vm2}, and G_{vm3} as derived in [10]. The ADC gain (K_{adc}), compensator (G_{cm}), and modulator gains (K_{M1}, K_{M2}, and K_{M3}) are all shown in Fig. 2. The total loop gain of the this loop is

$$\begin{aligned} T_{out} =& K_{adc}G_{cm} \\ & \big(K_{M1}G_{vm1} + K_{M2}G_{vm2} + K_{M3}G_{vm3}\big), \end{aligned} \tag{1}$$

where the constant gains and plant gains are known and compensator G_{cm} is designed for the desired bandwidth and phase margin characteristics.

B. Isolated Frequency Synchronization

Assuming the output remains perfectly regulated, the frequency synchronization control loop is shown in Fig. 3 where K_{dco} is the gain of the digitally controlled oscillator, K_{pfd} is that of the phase frequency detector, and G_{zp} models the dynamics of the power stage [10]. Phase-locked loop (PLL) compensator, G_{cp}, is designed for system stability. The loop gain of the PLL is

$$T_{pll} = K_{pfd}G_{cp}K_{dco}\frac{2\pi}{s}, \tag{2}$$

and the loop gain for all of Fig. 3, including power stage dynamics, is

$$T_{freq} = T_{pll}\big(G_{zp} - 1\big). \tag{3}$$

Like a conventional voltage control loop, the error term $\hat{\phi}_e$ is driven to zero. This phase-locked loop, informed by the power circuit plant model, forces the rectifier's switching phase (and consequent frequency) to converge to the WPT carrier established by the transmitter.

III. Complete System Derivation

In reality the two control loops interact with one another. A change in modulation index affects the phase of the system, and a change in the control phase affects the output voltage of the rectifier. These cross-coupling mechanisms are described in Fig. 4 by four additional plant models: G_{zm1}, G_{zm2}, G_{zm3}, and G_{vp} [10]. Gains K_{rad} and K_{vp} are unit conversions between radians and time: $K_{rad} = 2\pi \cdot 150$ kHz and $K_{vp} = 1/(2\pi \cdot 150$ kHz). The complete, cross-coupled system is modeled as linear time independent (LTI), and therefore, transfer functions from each of the inputs to each of the outputs exist. Fig. 4 shows the two system inputs ($\hat{v}_{ref}$ and $\hat{\phi}_{ref}$) and the two regulated output nodes ($\hat{v}_{out}$ and $\hat{\phi}_n$) in purple and red, respectively.

Subcircuit 1 in Fig. 4 is reduced such that local outputs are described in terms of the local inputs. That is, $\hat{d}_1$, $\hat{d}_2$, $\hat{d}_3$, and $\hat{v}_{out}$ are described in terms of $\hat{v}_{ref}$ and $\hat{v}_{outp}$. Subcircuit 2 has output $\hat{\phi}_{pwm}$ described in terms of $\hat{\phi}_{wpt}$ and $\hat{\phi}_{ref}$. These resulting subcircuit block diagrams are shown in Fig. 5, where blocks B_1-B_{10} are defined in Table I.

The subcircuit simplifications enable derivation of the final small signal model shown in Fig. 6. Next, $\hat{\phi}_{pwm}$ is solved in terms of the system-wide inputs. The solutions for $\hat{\phi}_{pwm}$ and $\hat{\phi}_{wpt}$ are given in Table II. The properties of LTI systems now allow either input to be set to zero, establishing the relationship from one input to one output without the need to assume either loop is ideal. The four solutions for the system are listed in Table II.

IV. Predicting Cross-Coupling Interactions

With the complete dual-loop system derived, comparison to the isolated designs reveals the effect of the cross-coupling

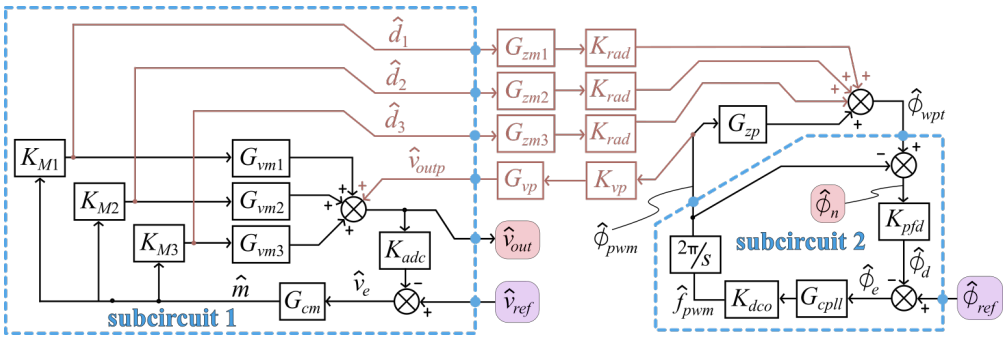

Fig. 4: The cross coupling effects of the four additional plant models on the two isolated control loops.

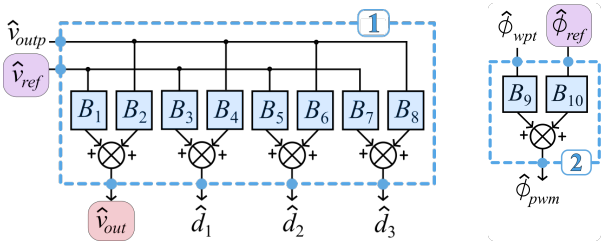

(a) (b)

Fig. 5: Reduced subcircuits (a) 1 and (b) 2 from Fig. 4.

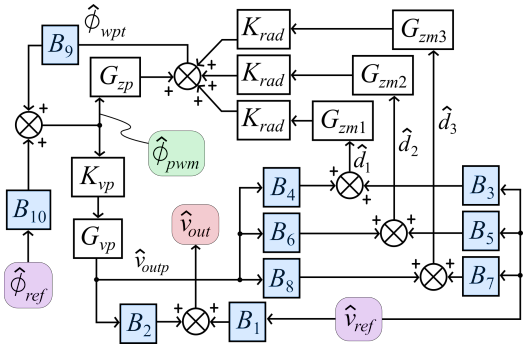

Fig. 6: Complete, reduced small signal representation of the MSC WPT dual-loop system.

TABLE I: Subcircuit Equations and Block Diagram Coefficients

Output	Equation	Subcircuit Blocks	
$\hat{v}_{out}$	$\hat{v}_{out} = \hat{v}_{ref}\ \frac{1}{K_{adc}}\ \frac{T_{out}}{1+T_{out}} + \hat{v}_{outp}\ \frac{1}{1+T_{out}}$	$B_1 = \frac{1}{K_{adc}}\ \frac{T_{out}}{1+T_{out}}$	$B_2 = \frac{1}{1+T_{out}}$
$\hat{d}_1$	$\hat{d}_1 = \hat{v}_{ref}\ \frac{K_{M1}G_{cm}}{1+T_{out}} - \hat{v}_{outp}\ \frac{K_{M1}G_{cd}K_{adc}}{1+T_{out}}$	$B_3 = \frac{K_{M1}G_{cm}}{1+T_{out}}$	$B_4 = -\frac{K_{M1}G_{cd}K_{adc}}{1+T_{out}}$
$\hat{d}_2$	$\hat{d}_2 = \hat{v}_{ref}\ \frac{K_{M2}G_{cm}}{1+T_{out}} - \hat{v}_{outp}\ \frac{K_{M2}G_{cd}K_{adc}}{1+T_{out}}$	$B_5 = \frac{K_{M2}G_{cm}}{1+T_{out}}$	$B_6 = -\frac{K_{M2}G_{cd}K_{adc}}{1+T_{out}}$
$\hat{d}_3$	$\hat{d}_3 = \hat{v}_{ref}\ \frac{K_{M3}G_{cm}}{1+T_{out}} - \hat{v}_{outp}\ \frac{K_{M3}G_{cd}K_{adc}}{1+T_{out}}$	$B_7 = \frac{K_{M3}G_{cm}}{1+T_{out}}$	$B_8 = -\frac{K_{M3}G_{cd}K_{adc}}{1+T_{out}}$
$\hat{\phi}_{pwm}$	$\hat{\phi}_{pwm} = \hat{\phi}_{ref}\ \frac{1}{K_{pfd}}\ \frac{T_{pll}}{1-T_{pll}} - \hat{\phi}_{wpt}\ \frac{T_{pll}}{1-T_{pll}}$	$B_9 = -\frac{T_{pll}}{1-T_{pll}}$	$B_{10} = \frac{1}{K_{pfd}}\frac{T_{pll}}{1-T_{pll}}$

TABLE II: Complete Small Signal Model

Derivations

$$\hat{\phi}_{pwm}\ (\hat{v}_{ref}, \hat{\phi}_{ref}) = \frac{\hat{\phi}_{ref}B_{10} + \hat{v}_{ref}\Big(B_9B_3K_{rad}G_{zm1} + B_9B_5K_{rad}G_{zm2} + B_9B_7K_{rad}G_{zm3}\Big)}{1 - \Big(B_9G_{zp} + B_9B_4K_{rad}G_{zm1}G_{vp}K_{vp} + B_9B_6K_{rad}G_{zm2}K_{vp}G_{vp} + B_9B_8K_{rad}G_{zm3}K_{vp}G_{vp}\Big)}$$

$$\hat{\phi}_{wpt} = \hat{\phi}_{pwm}\Big(G_{zp} - 1\Big) + K_{rad}G_{zm1}\Big(\hat{v}_{ref}B_3 + \hat{\phi}_{pwm}\ B_4K_{vp}G_{vp}\ \Big) + K_{rad}G_{zm2}\Big(\hat{v}_{ref}B_5 + \hat{\phi}_{pwm}\ B_6K_{vp}G_{vp}\ \Big) + K_{rad}G_{zm3}\Big(\hat{v}_{ref}B_7 + \hat{\phi}_{pwm}\ B_8K_{vp}G_{vp}\Big)$$

Final Solutions

$\hat{v}_{out} = \hat{\phi}_{pwm}\ (\hat{v}_{ref}, 0)B_2K_{vp}G_{vp} + \hat{v}_{ref}B_1$	$\hat{\phi}_n = \hat{\phi}_{wpt}(0, \hat{\phi}_{ref}) - \hat{\phi}_{pwm}\ (0, \hat{\phi}_{ref})\big(1 - B_4K_{vp}G_{vp}\big)$
$\hat{v}_{out} = \hat{\phi}_{pwm}\ (0, \hat{\phi}_{ref})B_2K_{vp}G_{vp}$	$\hat{\phi}_n = \hat{\phi}_{wpt}(\hat{v}_{ref}, 0) - \hat{\phi}_{pwm}\ (\hat{v}_{ref}, 0)\big(1 - B_4K_{vp}G_{vp}\big) + \hat{v}_{ref}B_3$

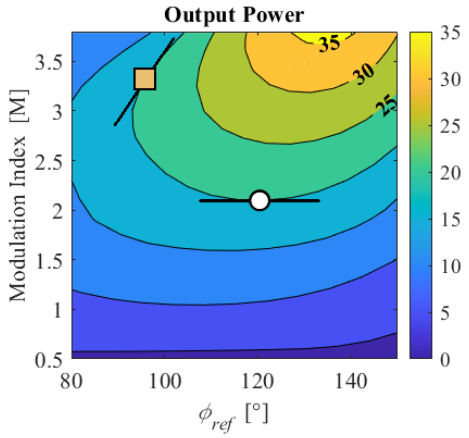

Fig. 7: Power contours for a WPT system tuned such that $L_{tx}|C_p = 50$ kHz and $L_{rx}|C_s = 131$ kHz. The data is calculated using a state-space based loss model with constant $V_{in} = 19$ V and $V_{out} = 5$ V for the WPT MSC system.

interactions. The isolated output regulation and frequency synchronization control loops have closed-loop gains of

$$T_{out,cl} = \frac{\hat{v}_{out}}{\hat{v}_{ref}} = \frac{1}{K_{adc}} \frac{T_{out}}{1 + T_{out}} \tag{4}$$

and

$$T_{freq,cl} = \frac{\hat{\phi}_n}{\hat{\phi}_{ref}} = \frac{1}{K_{pfd}} \frac{T_{freq}}{1 + T_{freq}}, \tag{5}$$

respectively. To evaluate the cross-coupling effects of the system, (4) and (5) are compared with the solutions derived in Table II.

The steady state power contours of the system can be used to predict the strength of cross-coupling interactions. To illustrate, the steady state values of output power are graphed for a detuned WPT tank with primary and secondary resonances of 50 kHz and 130 kHz (denoted $L_{tx}|C_p = 50$ kHz and $L_{rx}|C_s = 130$ kHz) in Fig. 7. The slope of the power contour at the white circle point is perpendicular to the modulation axis. Intuitively, this is beneficial because modulation is used to control power: a change in modulation near this point affects output power. Inversely, a change in ϕ_{ref} around this same operating point does not affect the steady state output power. The orange square in Fig. 7 demonstrates a different case, and a change in either M or ϕ_{ref} around this point varies the output power.

The small signal representations of the square and dot points from Fig. 7 are shown in Figs. 8a and 8b, respectively. For Fig. 8a, the loop gains T_{out} and T_{freq} are compensated to have similar bandwidths (4.5 kHz and 5.4 kHz). The complete closed-form solution derived in Table II predicts resonant dynamics that the isolated designs of Section II miss. For Fig. 8b, the same compensators are used, and the two small signal derivations show good agreement. Here, designing the two control loops in isolation is a valid strategy, but the same is not true of Fig. 8a.

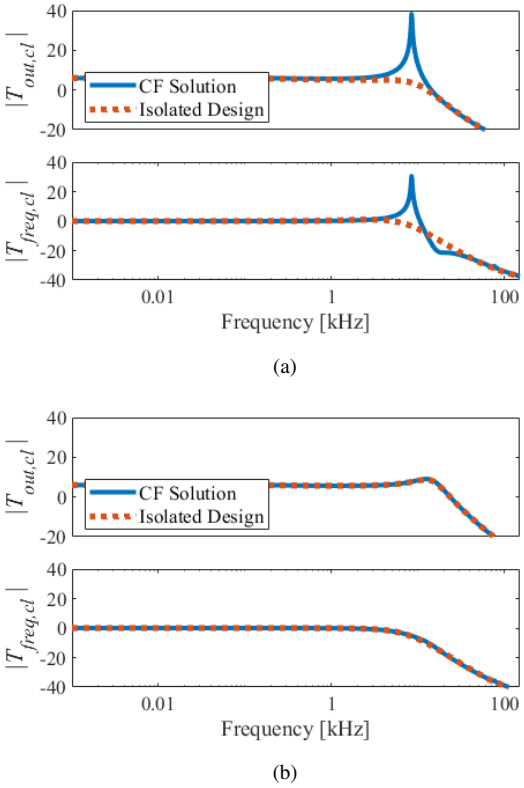

Fig. 8: Bode comparisons of the isolated and complete models for both the (a) orange square and (b) white circle points on Fig. 7.

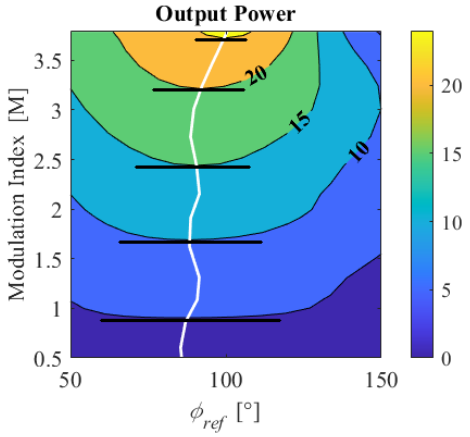

Fig. 9: Ideal experimental tuning: $L_{tx}|C_p = 150$ kHz and $L_{rx}|C_s = 150$ kHz. The white line is the optimal fundamental WPT load ($\angle Z_{rec} = 0$), and the black lines highlight the power contour slopes that attenuate cross-coupling interactions.

Per the analysis in Fig. 7 and 8, the design is made simpler if the operating points of the WPT rectifier lie within a region that inherently attenuates cross-coupling effects. Incidentally, these regions align with the desired steady state loading characteristics of WPT systems when the tank is tuned

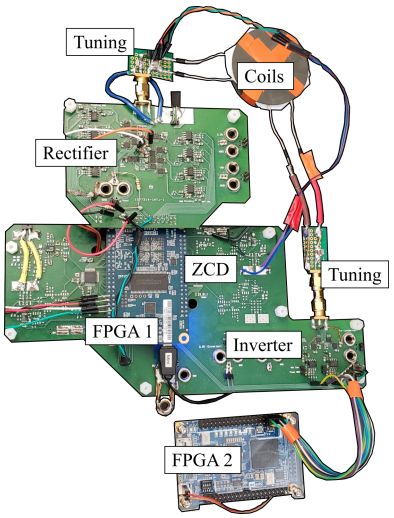

Fig. 10: Experimental prototype circuit with two FPGA controllers for synchronization testing.

TABLE III: Circuit Parameters

Parameter	Value		
L_{tx}	13.27 μH	L_{rx}	13.21 μH
C_p	111.01 nF	C_s	84.14 nF
R_p	79.15 mΩ	R_s	119.71 mΩ
Coupling, k	0.784	C_{fly}	15.66 μF
FETs	BSZ0910NDXTMA1	C_{out}	58.73 μF
Gate Driver	MP1907AGQ-P	V_{out}	5 V

ideally. Under the ideal tuning, the primary and secondary both resonate at the fundamental, that is: $L_{tx}|C_p = 150$ kHz and $L_{rx}|C_s = 150$ kHz. This case is shown in Fig. 9. Under the fundamental model, the maximum rectifier efficiency is the trajectory where the impedance presented by the rectifier is resistive (shown by the white line). This trajectory is perpendicular to the iso-power contours at all points, meaning that the highest efficiency and lowest cross-coupling trajectory are identical in the ideal tuning case. However, when the tank is detuned from the ideal case and items like harmonic content, sensing delays, and switching loss are considered, then the optimal trajectories for efficiency and cross-coupling attenuation will not precisely coincide.

V. Experimental Platform and Stability

The experimental prototype circuit is shown in Fig. 10. The components and circuit values that comprise the experimental platform are outlined in Table III. The flying capacitors (C_{fly}) are responsible for the 7-level modulation of the MSC. The two FPGA controllers shown in Fig. 10 enable the inverter and rectifier to be driven separately, thereby allowing for true synchronization testing without any direct communication.

To test the viability of wide-range dual-loop control for WPT rectification, two sets of tests are used to validate the analysis. First, dual-loop operation is verified with the WPT

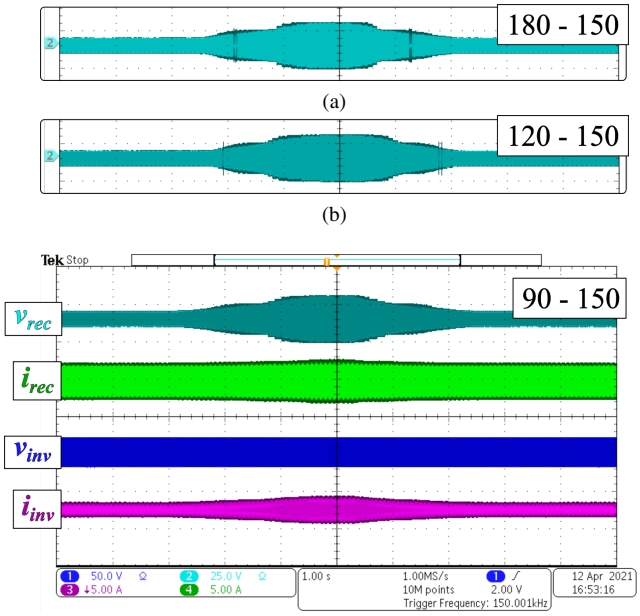

Fig. 11: Experimental power sweeps up to 20W for tanks with $L_{rx}|C_s = 150$ kHz and an $L_{tx}|C_p$ resonance of (a) 180 kHz, (b) 120 kHz, and (c) 90 kHz.

tank retuned in multiple ways. Second, the phase reference and output power are modulated simultaneously to ensure stable traversal of the operating space.

A. Operation under Primary-Side Detuning

If a designer tunes the secondary side at the fundamental frequency and appropriately compensates the synchronization and output loops, then the system must remain stable when paired to a primary side that is not tuned at the ideal resonant point. Given that the engineer designing the rectifier may not have control over the primary side design, stable operation in the presence of varying primary tuning is desirable.

Fig. 11 shows three oscilloscope captures for three different tests under dual-loop control. Each test uses a single value of ϕ_{ref} to traverse from low power up to 20 W. In each case, the WPT tank is retuned on the primary side, and the secondary side remains tuned at 150 kHz. Figs. 11a-11c have primary side tunings of 180, 120, and 90 kHz, respectively, but each test is conducted with a fundamental frequency of 150 kHz. In each case, the system remains stable with the output remaining regulated to 5 V at all powers. This demonstrates that even without ideal WPT tank tuning, the cross-coupling effects of dual-loop control are adequately attenuated.

B. Wide-Range Dual-Loop Stability

Finally, the values in Table III yield $L_{tx}|C_p = 131$ kHz and $L_{rx}|C_s = 150$ kHz. The power contour plot of this tank, including the zero slope lines, is shown in Fig. 12. Furthermore, the six operating points (white dots) highlighted in Fig. 12 coincide with Figs. 13 and 14, wherein each of

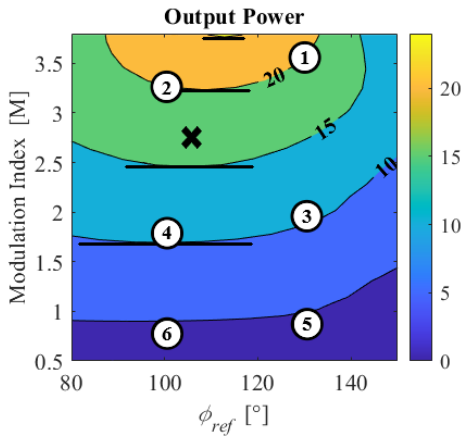

Fig. 12: Experimental tuning according to Table III.

these steady state points is displayed. The code is set to ramp linearly back and forth between $\phi_{ref} = 100.1°$ and $\phi_{ref} = 129.2°$ about every 1 second. The brief dip in V_{out} is the effect of a nearly 10 W load step from $R_{load} = 2.2\Omega$ to $R_{load} = 1.2\Omega$. This experimental range results in tested rectifier impedance magnitudes from 1.6 Ω to 6.7 Ω and tested rectifier impedance angles from 3° to 36°. The control loops are designed in isolation at the black X, resulting in a 6.88 kHz bandwidth and 56.1° phase margin for T_{out} and 1.47 kHz and 85.2° for T_{freq}. Fig. 13 shows that the dual-loop system remains stable over a wide range of loading conditions, allowing the rectifier to simultaneously retune the WPT system and regulate the output.

VI. Conclusions

The MSC rectifier requires two control loops for operation. Closed form equations for the complete dual-loop system are presented, and by comparison to the isolated designs, the need to consider such cross-coupled interactions is motivated. Steady state power contours are shown to imply areas of reduced cross-coupling, and the test platform shows both experimental stability with respect to primary side detuning and stable wide-range operation, given that the system is tuned near the ideal case. Stable control enables the MSC solution to simultaneously retune the WPT system and regulate the output.

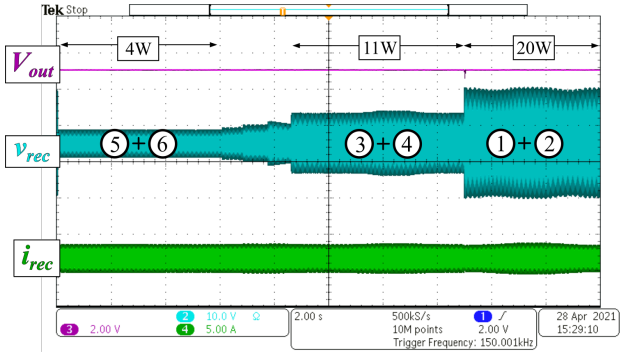

Fig. 13: Experimental waveforms traversing the six steady state operating points marked on Fig. 12.

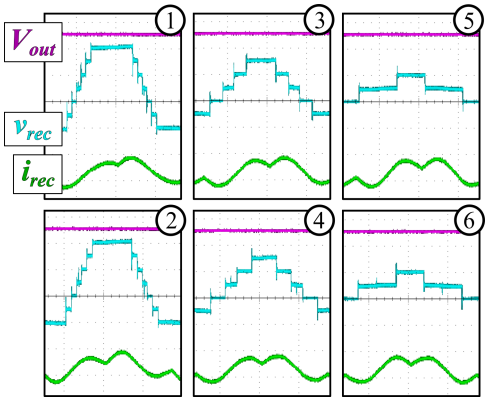

Fig. 14: Zoomed in waveforms of points 1-6.

References

[1] C. Zhao, D. Costinett, and S. Yang, "A seven-level switched capacitor ac-dc rectifier for fast wireless charging," in *2018 IEEE PELS Workshop on Emerging Technologies: Wireless Power Transfer (Wow)*, June 2018, pp. 1–6.

[2] A. Berger, M. Agostinelli, S. Vesti, J. A. Oliver, J. A. Cobos, and M. Huemer, "A wireless charging system applying phase-shift and amplitude control to maximize efficiency and extractable power," *IEEE Transactions on Power Electronics*, vol. 30, no. 11, pp. 6338–6348, Nov 2015.

[3] Young-Jun Park, SeongJin Oh, SangYun Kim, Sunghun Cho, MinChan Kim, Ju-Hyun Park, DongSoo Lee, HongJin Kim, and Kang-Yoon Lee, "A design of inductive coupling wireless power receiver with high efficiency active rectifier and multi feedback ldo regulator," in *2016 IEEE Wireless Power Transfer Conference (WPTC)*, 2016, pp. 1–4.

[4] K. Colak, E. Asa, and D. Czarkowski, "A novel phase control of single switch active rectifier for inductive power transfer applications," in *2016 IEEE Applied Power Electronics Conference and Exposition (APEC)*, 2016, pp. 1767–1772.

[5] C. Zhao, D. Costinett, and S. Yang, "A seven-level switched capacitor ac-dc rectifier for fast wireless charging," in *2018 IEEE PELS Workshop on Emerging Technologies: Wireless Power Transfer (Wow)*, 2018, pp. 1–6.

[6] Z. Xue, D. Li, W. Gou, L. Zhang, S. Fan, and L. Geng, "A delay time controlled active rectifier with 95.3% peak efficiency for wireless power transmission systems," in *2017 IEEE International Symposium on Circuits and Systems (ISCAS)*, May 2017, pp. 1–4.

[7] D. Wu, R. Mai, S. Zhao, Z. He, and F. Peng, "A self-oscillating controller based on pulse density modulator in wireless power transfer," in *2019 IEEE Energy Conversion Congress and Exposition (ECCE)*, 2019, pp. 2125–2128.

[8] A. Muramatsu and H. Nakamoto, "1.2-mm thin and compact direct ac-dc converter in wireless power receiver suitable for wearable devices," in *2019 IEEE Applied Power Electronics Conference and Exposition (APEC)*, 2019, pp. 841–845.

[9] E. Ozalevli, N. Femia, G. D. Capua, R. Subramonian, D. Du, J. Sankman, and M. E. Markhi, "A cost-effective adaptive rectifier for low power loosely coupled wireless power transfer systems," *IEEE Transactions on Circuits and Systems I: Regular Papers*, vol. 65, no. 7, pp. 2318–2329, July 2018.

[10] S. Cochran and D. Costinett, "Dual-loop frequency synchronization and load regulation using a discrete time model for a 7-level switched capacitor wpt rectifier," in *2020 IEEE 21st Workshop on Control and Modeling for Power Electronics (COMPEL)*, 2020, pp. 1–8.

[11] C. Zhao, S. Cochran, D. Costinett, and S. Yang, "Design and evaluation of a multilevel switched capacitor rectifier for wireless fast charging," in *2019 IEEE Applied Power Electronics Conference and Exposition (APEC)*, 2019, pp. 833–840.